nature materials

Article

https://doi.org/10.1038/s41563-023-01496-2

Intercell moiré exciton complexes in electron lattices

Received: 13 May 2022

Accepted: 1 February 2023

Published online: 09 March 2023

Check for updates

Xi Wang[1,2,10], Xiaowei Zhang[3,10], Jiayi Zhu[1,10], Heonjoon Park[1,10], Yingqi Wang[1], Chong Wang[3], William G. Holtzmann[1], Takashi Taniguchi[4], Kenji Watanabe[5], Jiaqiang Yan[6], Daniel R. Gamelin[2], Wang Yao[7,8] ✉, Di Xiao[3,1,9] ✉, Ting Cao[3] ✉ & Xiaodong Xu[1,3] ✉

Excitons, Coulomb-bound electron–hole pairs, play a crucial role in both optical excitation and correlated phenomena in solids. When excitons interact with other quasiparticles, few- and many-body excited states can appear. Here we report an interaction between exciton and charges enabled by unusual quantum confinement in two-dimensional moiré superlattices, which results in many-body ground states composed of moiré excitons and correlated electron lattices. In an H-stacked (60°-twisted) WS_2/WSe_2 heterobilayer, we found an interlayer moiré exciton whose hole is surrounded by its partner electron's wavefunction distributed among three adjacent moiré traps. This three-dimensional excitonic structure enables large in-plane electrical quadrupole moments in addition to the vertical dipole. Upon doping, the quadrupole facilitates the binding of interlayer moiré excitons to the charges in neighbouring moiré cells, forming intercell charged exciton complexes. Our work provides a framework for understanding and engineering emergent exciton many-body states in correlated moiré charge orders.

In two-dimensional semiconducting moiré superlattices, such as $MoSe_2$/WSe_2 and WS_2/WSe_2, the superlattice potential results in arrays of trapping sites, giving rise to a class of elementary photoexcitation—moiré excitons[1–6]. Due to the type-II band alignment of the host heterostructure, the ground-state moiré excitons consist of electrons and holes localized in opposite layers[7]. The interlayer moiré excitons possess unique physical properties, such as layer-stacking-dependent optical selection rules and Landé *g*-factors[1], coupled spin–valley pseudospin degrees of freedom[8,9], arrays of interacting single emitters[2,10] and synthetic gauge fields for possible topological excitonic lattices[10]. However, semiconducting moiré superlattices are also powerful laboratories for exploring tunable many-body electronic ground states due to exceptionally strong Coulomb interactions[11–23]. Therefore, these moiré superlattices offer an opportunity to explore the interplay of moiré excitons with a correlated charge background.

Interlayer moiré excitons have been used to sense correlated charge states. A simple correlation between the enhancement of photoluminescence (PL) and the formation of both integer and fractionally filled moiré minibands has been well established[15,16,21,24]. However, little is known about how interlayer moiré excitons interplay with the variety of charge orders, and thus the resulting correlated states of the interacting exciton–electron lattice system. For instance, is the

[1]Department of Physics, University of Washington, Seattle, WA, USA. [2]Department of Chemistry, University of Washington, Seattle, WA, USA. [3]Department of Materials Science and Engineering, University of Washington, Seattle, WA, USA. [4]International Center for Materials Nanoarchitectonics, National Institute for Materials Science, Tsukuba, Japan. [5]Research Center for Functional Materials, National Institute for Materials Science, Tsukuba, Japan. [6]Materials Science and Technology Division, Oak Ridge National Laboratory, Oak Ridge, TN, USA. [7]Department of Physics, University of Hong Kong, Hong Kong, China. [8]HKU-UCAS Joint Institute of Theoretical and Computational Physics at Hong Kong, Hong Kong, China. [9]Pacific Northwest National Laboratory, Richland, WA, USA. [10]These authors contributed equally: Xi Wang, Xiaowei Zhang, Jiayi Zhu, Heonjoon Park. ✉e-mail: wangyao@hku.hk; dixiao@uw.edu; tingcao@uw.edu; xuxd@uw.edu

https://doi.org/10.1038/s41563-023-01496-2

interaction between exciton and moiré trapped charges similar to the simple trion picture, that is, a neutral exciton bound to an extra charge? Or is there a new type of many-body excited state formed as the moiré excitons are embedded in the electron lattice? Understanding these fundamental questions will provide a framework for the burgeoning field of interacting opto-moiré quantum matter[11–21] and for the field of strongly correlated phenomena in optical excitations[25].

Here we discover a class of ground-state moiré excitons that can simultaneously possess a large in-plane quadrupole and out-of-plane dipole moment, creating a 3D structure in the H-stacked heterobilayer. By sequentially charging the moiré traps, the developing in-plane quadrupole moment enables the binding of such a moiré exciton to the ordered charges localized in the neighbouring moiré cells, forming an intercell charged moiré exciton complex—a special type of many-body excitonic state. Distinct from trion[26–28] and exciton–Fermi polaron physics[29], the intercell moiré exciton complex manifests as replica of the exciton PL spectral features as a function of doping. We find tens of meV blueshift in the moiré exciton PL peaks across the integer moiré filling, resulting from intracell Coulomb repulsion, and a subsequent 5–10 meV redshift as the moiré minibands are fractionally filled. The latter value corresponds to the binding energy of the intercell moiré exciton complex.

Moiré spatial charge distribution

The moiré electronic structure sensitively depends on layer stacking and local interlayer atomic registry. We performed density-functional theory calculations to capture such dependence (Methods). Figure 1a,b depicts an R- and H-stacked moiré supercell, respectively, with three high-symmetry positions marked as A, B and C. Using R stacking as an example, the A, B and C regions have local stacking arrangements of R^h_h, R^M_h and R^X_h, respectively. The notation R^μ_h represents the μ (μ = h (hollow), M (W), X (S)) site of the electron layer (WS_2) vertically aligned with the hexagonal centre h of the bottom hole layer WSe_2. To capture the significant lattice reconstruction in the moiré superlattices[30], we performed structural relaxation calculations and found different strain distribution between R- and H-stacked heterobilayers (Extended Data Fig. 1a,b,d,e). This distinct feature is due to the different structural energy distributions of local stacking (Extended Data Fig. 1c,f).

Based on these reconstructed moiré structures, we calculate the spatial wavefunction of the valley-moiré conduction band bottom and valence band top, corresponding to the expected positions of the frontier electron- and hole-orbitals, respectively. For R stacking, both the electron and hole are localized at C (Fig. 1c). Therefore, for the ground-state moiré exciton, the electron in the WS_2 layer is vertically aligned with the hole in the WSe_2 layer, that is, there is no lateral misalignment between the electron and hole wavefunctions. The moiré exciton ground state is thus expected to only have an appreciable out-of-plane electric dipole.

In contrast, the wavefunction in the H-stacked heterobilayer has very different spatial distributions. While the hole is largely localized at C, the electron is mostly localized at a different region, A. For the ground-state moiré exciton, the electron and hole wavefunction are thus expected to be vertically misaligned. For a fixed hole at C in WSe_2, the bound electron wavefunction is expected to spread over three adjacent A positions of the WS_2 layer with a 3-fold rotational symmetry (Fig. 1d). As we will discuss next, this exciton wavefunction features both in-plane electric quadrupole and out-of-plane dipole moments, which lead to the formation of a new class of intercell moiré exciton complex in the presence of the electron lattice (correlated charge order).

Layer-stacking-dependent photoluminescence

In our experiment, we fabricated both R- and H-stacked WS_2/WSe_2 heterobilayers (Methods). Figure 2a–c shows optical microscopy, atomic force microscopy (AFM) and piezoresponse force microscopy (PFM) images of a representative H-stacked sample with 7.6 nm moiré wavelength. We performed PL measurements of interlayer moiré excitons.

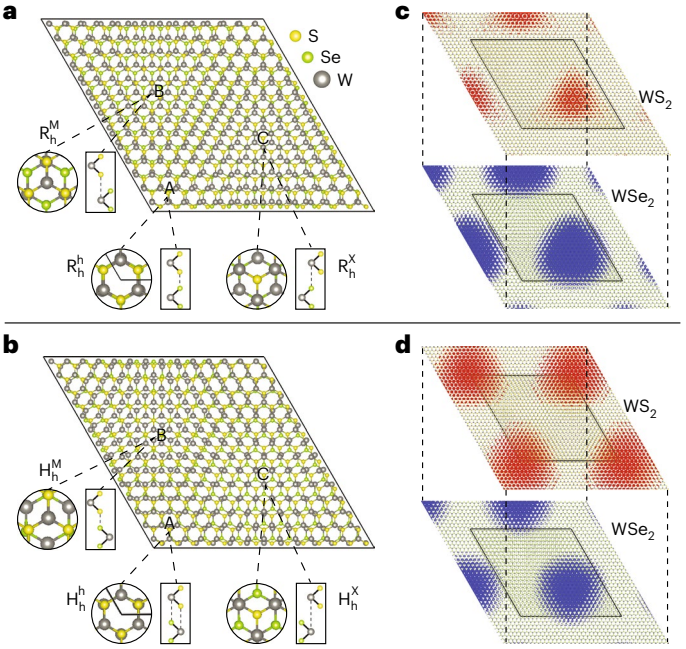

Fig. 1 | Spatial charge distribution of interlayer moiré exciton. a, Schematic of R-stacked WS_2/WSe_2 (top/bottom) heterobilayer. Zoom-in plots show the atomic registry of three high-symmetry positions in the moiré supercell, A, B, C, corresponding to local stacking arrangements R^μ_h. The true structure employed in the first-principles calculations has 3,903 atoms per moiré supercell, larger than the cell size shown in **a**, which exaggerates the moiré lattice mismatch for illustration. **b**, Similar plot as **a** but for H-stacked heterobilayer. **c**,**d**, Calculated spatial Kohn–Sham wavefunction of the valley-moiré conduction band bottom and valence band top in R-stacked (**c**) and H-stacked (**d**) heterobilayers, illustrating the expected spatial distributions of band-edge electrons and holes, respectively. Isosurface of squared wavefunction is taken at ~2% of its maximum value. For R stacking, both the electron and hole are localized at C. Therefore, for the ground-state moiré exciton, the electron in the WS_2 layer is vertically aligned with the hole in the WSe_2 layer (**c**). In contrast, in the H-stacked heterobilayer, while the hole is localized at C, the electron is mostly localized at A. For the ground-state moiré exciton with a fixed hole at C in WSe_2, the bound electron wavefunction largely spreads among the three adjacent A positions of the WS_2 layer (**d**). Therefore, in addition to the out-of-plane dipole, the interlayer moiré exciton has an in-plane electric quadrupole moment.

The optical excitation power is kept low (50 nW) to avoid possible optical doping effects, and the excitation energy is specified in the figure captions. Figure 2d shows the PL spectrum of an R-stacked heterobilayer at charge neutral (Device R1) at 10 K. A pronounced interlayer exciton PL peak is observed at ~1.37 eV, consistent with previous reports[3,15,16].

We then measured interlayer moiré exciton PL as a function of doping with the electric field fixed at zero. Figure 2e shows the results from Device R1 with the filling factor υ as indicated (see Methods and Extended Data Fig. 2 for the assignment of υ). The data are plotted in log scale to highlight the weak features for $|\upsilon| > 1$. Linecuts at select filling factors are shown in Extended Data Fig. 3. The PL exhibits sharp intensity jumps as doping reaches both fractional and integer filled moiré minibands, due to the formation of charge-ordered states. Near each fractional filling factor, the interlayer exciton PL intensity plot as a function of doping and emission energy shows sharp tilted line features. Since the peak energy along the tilted line always blueshifts for either increasing electron or hole doping, this rules out the possible Stark effect as its cause due to unbalanced top and bottom gates. Instead, we speculate that the charge-ordered states are robust even with a small number of excess electrons. The excess electrons can act as a screening cloud until the number of electrons meets the requirement

https://doi.org/10.1038/s41563-023-01496-2

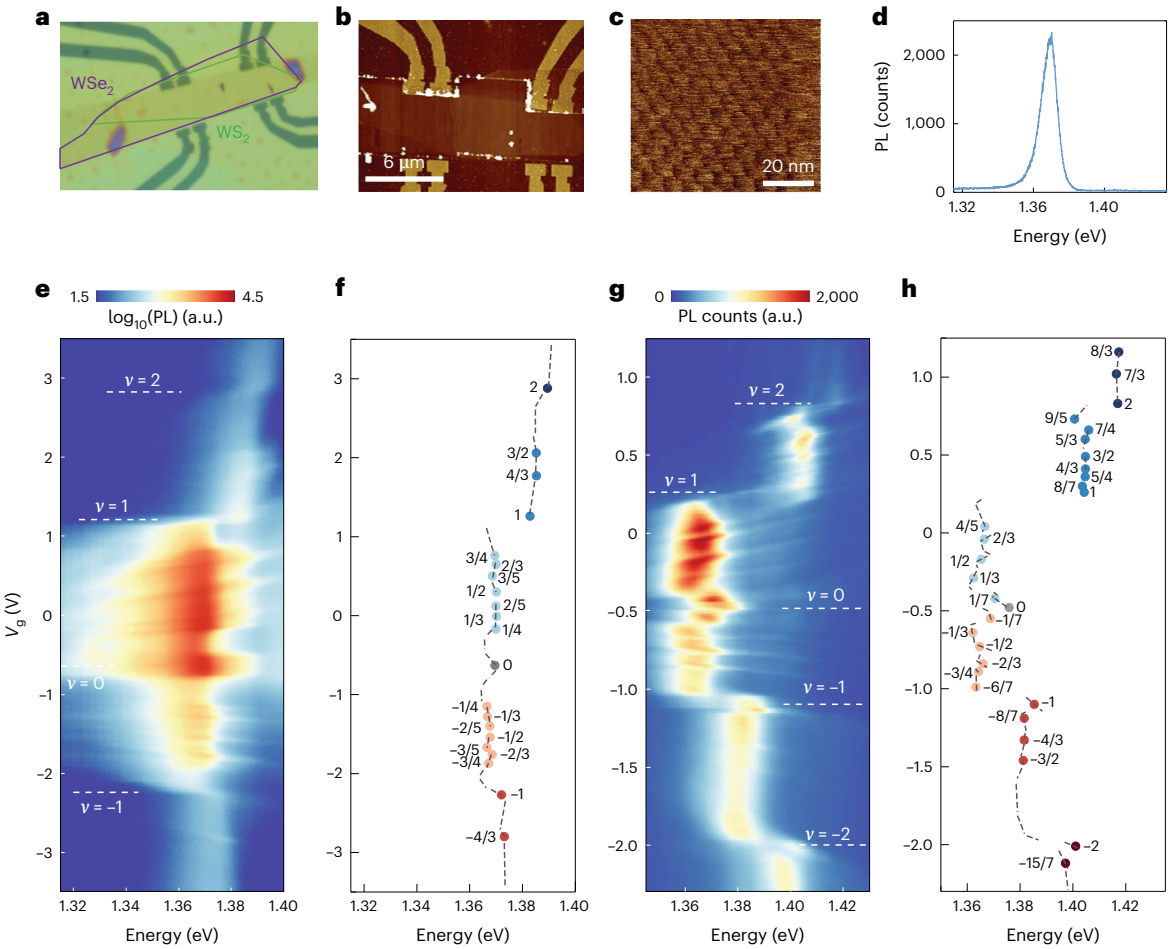

Fig. 2 | Moiré exciton PL in the presence of correlated charge orders. **a**, Optical microscopy image of a near-60° twisted WS_2/WSe_2 heterobilayer. **b**, Corresponding AFM image. **c**, PFM image, showing moiré pattern with a triangular lattice. **d**, PL spectrum of an interlayer moiré exciton of an R-stacked device (Device R1). **e**, Interlayer exciton PL intensity plot (log scale) versus moiré filling factor υ of Device R1. Optical excitation is 1.678 eV with 50 nW power. **f**, Extracted PL peak energies (dots) for each integer and fractionally filled correlated charge states. The dashed lines indicate PL peak energies at all measured gate voltages. **g**,**h**, The same plots as **e** and **f** but for the H-stacked Device H1. Optical excitation is 1.96 eV with 50 nW power. See text for details.

to form another correlated insulating state at a new fractional filling. The precise slope of the diagonal features is determined by the filling-factor-dependent local dielectric environment of each device.

We extract the PL peak energies at those most appreciable charge-ordered states and plot them versus υ in Fig. 2f. The dashed lines represent the peak energies at all measured gate voltages. Relative energy shifts at corresponding fractional and integer fillings are plotted in Extended Data Fig. 4a. Among the fractional υ states between two consecutive integer υ, the energy of PL peaks varies little (Fig. 2e,f). As $|\upsilon|$ goes across an integer value, the peaks blueshift. For instance, the blueshift is about 5 and 17 meV, respectively, as υ crosses −1 and 1 (corresponding to the charge-ordered states with one hole and one electron per moiré unit cell). Extended Data Figs. 5 and 6 show similar measurements of additional R-stacked heterobilayer devices. Although some details differ (such as the number of observed correlated charge orders), probably due to sample-to-sample variations, the dependence of the PL peak energy as a function of υ is consistent. The observation is distinct from that in $MoSe_2/WSe_2$ heterobilayer, where moiré exciton PL peaks have a discrete redshift by about 7 meV upon formation of moiré trions by doping[26–28].

In contrast, H-stacked samples show drastically different doping dependence of the exciton PL. Figure 2g shows the PL intensity plot with integer filling factors indicated (Extended Data Fig. 2). The extracted PL peak energies of prominent charge-ordered states are plotted in Fig. 2h. Relative energy shifts are shown in Extended Data Fig. 4b. Over two dozen correlated states at both integer and fractional moiré fillings are observed. Despite similar jumps of PL intensity at these fillings, the dependence of peak energy on υ is distinct in H-stacked samples compared to the R-stacked ones. Starting from charge neutrality, the first charge order appears at fractional moiré filling $\upsilon = \pm 1/7$. This is evident from the enhanced PL intensity and sudden peak redshifts of about 5 meV (v = 1/7) and 7 meV (v = −1/7) (Extended Data Fig. 7). Here, $|v| = 1/7$ corresponds to a commensurate triangular charge lattice. When the next charge order at $\upsilon = \pm 1/3$ forms, further redshifts of 8 meV ($\upsilon = 1/3$) and 7 meV ($\upsilon = -1/3$) are observed. These discrete redshifts are missing in all R-stacked samples in the same doping range. Upon further doping, PL peak energies have little variation until reaching v = ±1, where the PL peaks exhibit sharp energy jumps by +22 and +42 meV for the $\upsilon = -1$ and +1 states, respectively. Similar to the peak redshift going from charge neutrality to $|v| = 1/7$, the PL peak redshifts again when $|\upsilon|$ is slightly larger than 1 to form the next fractionally filled state. This redshift is most pronounced from v = −1 to −8/7 of about 4 meV. The general spectral feature between $1 \le |\upsilon| < 2$ resembles that between $0 \le |\upsilon| < 1$ despite fine differences, such as the number of observed correlated states.

When $|\upsilon|$ exceeds 2, the spectral dependence on υ is most appreciable on the hole side. The PL peak first blueshifts for another 18 meV at $\upsilon = -2$, and then exhibits discrete redshifts of about 4 meV as doping increases slightly. Upon further doping, the peak continues to blueshift. This behaviour for υ over −2 again resembles those of $0 \le |\upsilon| < 1$, except that

https://doi.org/10.1038/s41563-023-01496-2

the signatures of correlated states are not clear, probably due to effective screening of long-range Coulomb interactions at high doping. Extended Data Fig. 8 shows similar measurements of an additional H-stacked heterobilayer device. Note that the R- and H-stacked samples in Extended Data Figs. 6 and 8 are from the different parts of the same device, that is, fabricated simultaneously. This further confirms the observation is due to stacking, rather than from device fabrication variation.

Intercell moiré exciton complex

The above experimental observations reveal the stacking-dependent interactions between interlayer excitons and electron lattice in moiré heterostructures. Figure 3a illustrates the key idea. Upon doping, moiré sites are fractionally filled. To avoid double occupancy and onsite Coulomb interactions, the interlayer exciton will only occupy an empty moiré site. As presented earlier, for a R-stacked heterobilayer, the electron and hole of the interlayer moiré exciton are vertically aligned, leading to a weakly repulsive interaction between the excitonic dipole and its adjacent moiré trapped charge (Fig. 3a, top panel). Thus, this interlayer exciton does not bind to the moiré charges. The fractional insulating states largely behave as an inert background and the PL peak energy experiences little variation with an estimated blueshift of <2 meV until integer filling (Methods and Extended Data Fig. 9).

In contrast, a large electric quadrupole can form for interlayer moiré excitons in the H-stacked heterobilayer (Fig. 3a, bottom panel), allowing the exciton to bind to the electron lattice. At $\upsilon = -1/7$, the dilute hole lattice regime, the interlayer exciton in an empty moiré cell can bind with the hole in the adjacent cell (Fig. 3b). This nearest-neighbour intercell Coulomb binding results in the observed ~7 meV redshift of PL peaks, consistent with the theoretical estimation (Extended Data Fig. 9). As the hole density increases, the interlayer exciton then interacts with the entire electron lattice, forming a charged intercell moiré exciton complex with an additional redshift. Figure 3c illustrates the intercell moiré exciton complex at $\upsilon = -1/3$. The observed PL peak energy difference between $|\upsilon| = 1/3$ and charge neutral thus corresponds to a binding energy of the intercell moiré exciton complex of ~14 meV, consistent with the estimate of 15 meV from theory (Extended Data Fig. 9). For filling factors larger than $|\upsilon| = 1/3$, the data suggest that the binding energy does not change significantly. The complicated interactions between exciton and doped electrons/holes may provide an overall screening effect, which result in a slight blueshift with doping.

With one hole in each moiré unit cell ($\upsilon = -1$), the interlayer moiré exciton interacts with an intra-moiré cell hole (Fig. 3d). The interaction involves both intracell hole–hole repulsion and electron–hole attraction, which have opposite signs. Since the electron and hole wavefunction are laterally misaligned in an H-stacked heterobilayer, this has a larger electron–hole separation than that in the R-stacked heterobilayer with vertically aligned electron–hole wavefunctions. Therefore, the excitonic Coulomb binding in the former is weaker than in the latter. Upon formation of a sizable charge gap at integer filling, this difference leads to a much larger increase of the PL peak energy (~22 meV at $\upsilon = -1$) in the H-stacked sample than that in the R-stacked heterobilayer (~5 meV). Upon further doping, the interlayer exciton will then again bind to the additional hole in the adjacent moiré site, forming a charged intercell moiré exciton. The above-described process repeats itself at either electron or hole integer moiré filling. Note that the energy jump at $\upsilon = 1$ is ~42 meV, larger than that for the $\upsilon = -1$ state. This asymmetry between the electron lattice and hole lattice may arise from dissimilar electron and hole wavefunctions of the interlayer exciton, which leads to different intracell Coulomb interaction strength.

Optical selection rules

We find layer-stacking-dependent PL polarization of the interlayer moiré exciton. Figure 4a,b shows the circular-polarization-resolved photoluminescence of the R-stacked heterobilayer (Device R1) and the associated degree of polarization as a function of doping. The optical

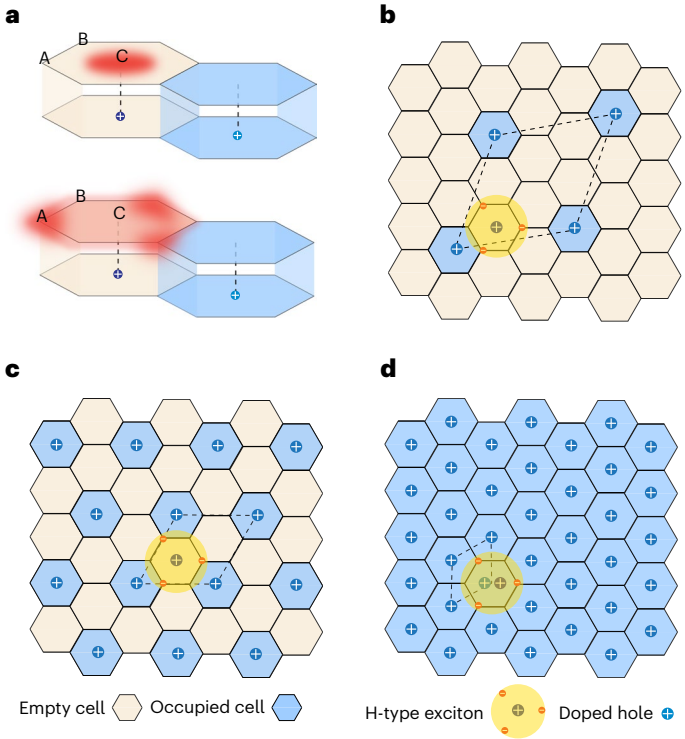

Fig. 3 | Schematics of intercell moiré exciton complexes. a, Cartoons depicting the interlayer exciton and an additional hole trapped in the adjacent moiré unit cell. In R stacking (top panel), because the electron and hole wavefunctions are vertically aligned, the moiré interlayer exciton has a weak repulsive interaction with the hole. In contrast, the exciton in H stacking (bottom panel) can have an attractive interaction with the hole by developing a large electric quadrupole that lies in-plane. The estimation of moiré exciton binding energies can be found in Supplementary Information, section 1. The red shading indicates the emission of excitons at preferred locations. **b**–**d**, Cartoons of intercell moiré exciton complexes for hole filling factors of $\nu = -1/7$ (**b**), $\nu = -1/3$ (**c**) and $\nu = -1$ (**d**) in an H-stacked heterobilayer. The light yellow (empty site) and light blue (with one doped hole) hexagons denote the Wigner–Seitz cell of the moiré primitive unit cell. The dashed parallelogram indicates the primitive unit cell of the hole lattice. For $\nu = -1$, intracell Coulomb interactions exist between the moiré exciton and the doped hole. Doped holes are labelled as blue circles with + signs. H-type excitons are indicated by the yellow circular shades; orange dots represent surrounded electrons.

excitation energy is 1.678 eV, in resonance with the WSe_2 1*s* exciton. PL is in general co-circularly polarized, but is cross-circularly polarized for υ beyond −1/2. Extended Data Fig. 10 shows similar measurement but with an 8 T out-of-plane magnetic field. The cross-polarized feature for $\nu < -1$ remains, implying the selection rule is determined by the symmetry of the local atomic registry. For the states of υ between +1 and −1, the degree of circular polarization is weak, while for $\upsilon > 1$, PL is strongly co-circularly polarized. In contrast, the H-stacked heterobilayer possesses distinct optical selection rules. Figure 4c shows the circular-polarization-resolved PL measurements as a function of doping (taken at a different spot and cool-down cycle compared to the data in Fig. 2). The corresponding degree of circular polarization is shown in Fig. 4d. The charge-neutral interlayer moiré exciton and the intercell moiré exciton complex are both cross-circularly polarized, although the degree of polarization is weak for $|\upsilon| < 1$. Consistent polarization-resolved measurements from additional R- and H-stacked samples are presented in Extended Data Figs. 6 and 8, respectively.

The distinct doping dependence of PL polarization is ascribed to the different atomic registries between the R- and H-stacked heterobilayers. The optical selection rule for interlayer electron–hole recombination is determined by both their spin–valley indices and the local

https://doi.org/10.1038/s41563-023-01496-2

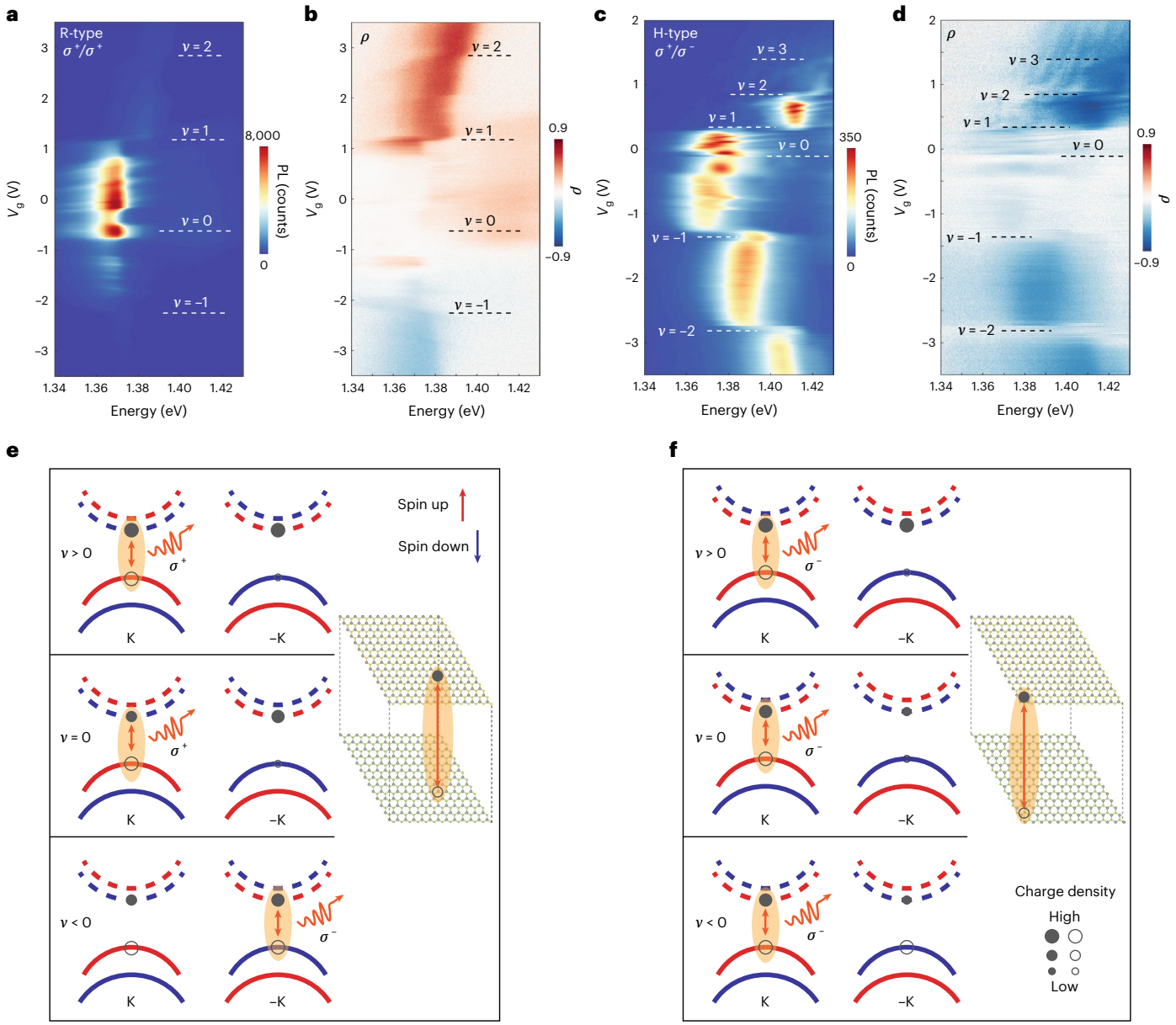

Fig. 4 | Stacking-dependent moiré exciton valley polarization. a,**c**, Co-circularly polarized interlayer exciton PL for Device R1 (**a**) and cross-circularly polarized interlayer exciton PL for Device H1 (**c**), under $\sigma+$ circularly polarized excitation. The excitation energy is in resonance with the WSe_2 1*s* exciton (~1.678 eV). The excitation power is 50 nW for R1 and 150 nW for H1. **b**,**d**, The corresponding degree of circular polarization $\rho = \frac{\sigma^+/\sigma^+ - \sigma^+/\sigma^-}{\sigma^+/\sigma^+ + \sigma^+/\sigma^-}$. **e**,**f**, Schematics of doping-dependent PL polarization for R-stacked (**e**) and H-stacked (**f**) heterobilayers. Solid (open) circles denote electrons (holes) with the circle size indicating the population. Solid (dashed) parabolas represent valence (conduction) bands from WSe_2 (WS_2), with red and blue denoting spin up and down, respectively. The PL polarization is determined by the majority-carrier valley index and the location of recombination in the moiré cell. As indicated by the insets, the electron and hole recombine at R_h^X for the R stacking, and mainly at H_h^h for the H stacking. See text for details.

stacking registry[31]. Below we illustrate the physical picture under $\sigma+$ polarized excitation with details given in Supplementary Information, section 2 and Supplementaty Figs. 1, and 2. As shown in Fig. 4e, for the R stacking, the electron and hole recombine at R_h^X, and the K valley of WSe_2 is nearly momentum-aligned with the K valley of WS_2. After $\sigma+$ pump, the photogenerated electron at the K valley of WSe_2 can relax into the K and −K valleys through spin-flip and valley-flip scattering. Previous works have shown that the relaxation rates for these two paths are similar[28,32]. In both charge-neutral and electron-doped cases, since the hole predominantly populates at the WSe_2 K valley, the emission helicity is $\sigma+$. In the hole-doped case, the hole has a comparable population at WSe_2 ±K valleys. In addition, noting that the population of photogenerated electrons at the WS_2 −K valley is likely to dominate over the K valley population, the polarization is reversed at a certain hole-doping level.

For H stacking, the K valley of WSe_2 is nearly momentum-aligned with the −K valley of WS_2, as shown in Fig. 4f. The photogenerated electron at the K valley of WSe_2 can efficiently tunnel into the bottom conduction band at the −K valley of WS_2 with both spin and momentum conservation. Due to lateral separation of electrons and holes, excitons can recombine at H_h^h or H_h^X, which have an opposite selection rule with the same spin configuration. Around charge neutrality, the observed small cross-polarization indicates that the recombination is more likely to be at H_h^h (A site). Since the dominant recombination site and optical transition do not change in both the electron-doped and hole-doped conditions, the emission helicity remains as $\sigma-$.

Summary

Our work reveals an exceptional stacking-dependent interlayer moiré exciton wavefunction, which leads to repulsive and attractive exciton–moiré carrier interactions in R- and H-stacked heterobilayers, respectively. This provides a framework for understanding interlayer moiré exciton properties, such as luminescence energy and valley polarization, in the presence of a multitude of correlated charge orders. The in-plane electrical quadruple moment of the interlayer exciton in the H-stacked sample enables its binding with the electron lattice to form a special type of exciton many-body ground state, with observed binding energy ~14 meV at 1/3 hole filling consistent with our theory. These findings will facilitate future work in unravelling and manipulating light–matter interactions in the rapidly developing field of semiconducting moiré quantum matter, which has emerged as a powerful platform to study correlated and topological phenomena with high degrees of tunability[11–23,33–39].

Online content

Any methods, additional references, Nature Portfolio reporting summaries, source data, extended data, supplementary information, acknowledgements, peer review information; details of author contributions and competing interests; and statements of data and code availability are available at https://doi.org/10.1038/s41563-023-01496-2.

References

1. Seyler, K. L. et al. Signatures of moiré-trapped valley excitons in $MoSe_2/WSe_2$ heterobilayers. *Nature* **567**, 66–70 (2019).
2. Baek, H. et al. Highly energy-tunable quantum light from moiré-trapped excitons. *Sci. Adv.* **6**, eaba8526 (2020).
3. Jin, C. et al. Observation of moiré excitons in WSe_2/WS_2 heterostructure superlattices. *Nature* **567**, 76–80 (2019).
4. Tran, K. et al. Evidence for moiré excitons in van der Waals heterostructures. *Nature* **567**, 71–75 (2019).
5. Alexeev, E. M. et al. Resonantly hybridized excitons in moiré superlattices in van der Waals heterostructures. *Nature* **567**, 81–86 (2019).
6. Zhang, N. et al. Moiré intralayer excitons in a $MoSe_2/MoS_2$ heterostructure. *Nano Lett.* **18**, 7651–7657 (2018).
7. Rivera, P. et al. Observation of long-lived interlayer excitons in monolayer $MoSe_2$–WSe_2 heterostructures. *Nat. Commun.* **6**, 6242 (2015).
8. Yu, H., Wang, Y., Tong, Q., Xu, X. & Yao, W. Anomalous Light Cones And Valley Optical Selection Rules Of Interlayer Excitons In Twisted Heterobilayers. *Phys. Rev. Lett.* **115**, 187002 (2015).
9. Rivera, P. et al. Interlayer valley excitons in heterobilayers of transition metal dichalcogenides. *Nat. Nanotechnol.* **13**, 1004–1015 (2018).
10. Yu, H., Liu, G.-B., Tang, J., Xu, X. & Yao, W. Moiré excitons: from programmable quantum emitter arrays to spin-orbit–coupled artificial lattices. *Sci. Adv.* **3**, e1701696 (2017).
11. Regan, E. C. et al. Mott and generalized Wigner crystal states in WSe_2/WS_2 moiré superlattices. *Nature* **579**, 359–363 (2020).
12. Xu, Y. et al. Correlated insulating states at fractional fillings of moiré superlattices. *Nature* **587**, 214–218 (2020).
13. Tang, Y. et al. Simulation of Hubbard model physics in WSe_2/WS_2 moiré superlattices. *Nature* **579**, 353–358 (2020).
14. Huang, X. et al. Correlated insulating states at fractional fillings of the WS_2/WSe_2 moiré lattice. *Nat. Phys.* https://doi.org/10.1038/s41567-021-01171-w (2021).
15. Miao, S. et al. Strong interaction between interlayer excitons and correlated electrons in WSe_2/WS_2 moiré superlattice. *Nat. Commun.* **12**, 3608 (2021).
16. Liu, E. et al. Excitonic and valley-polarization signatures of fractional correlated electronic phases in a WSe_2/WS_2 moiré superlattice. *Phys. Rev. Lett.* **127**, 037402 (2021).
17. Shimazaki, Y. et al. Strongly correlated electrons and hybrid excitons in a moiré heterostructure. *Nature* **580**, 472–477 (2020).
18. Zhou, Y. et al. Bilayer Wigner crystals in a transition metal dichalcogenide heterostructure. *Nature* **595**, 48–52 (2021).
19. Li, H. et al. Imaging two-dimensional generalized Wigner crystals. *Nature* **597**, 650–654 (2021).
20. Wu, F., Lovorn, T., Tutuc, E. & MacDonald, A. H. Hubbard model physics in transition metal dichalcogenide moiré bands. *Phys. Rev. Lett.* **121**, 026402 (2018).
21. Jin, C. et al. Stripe phases in WSe_2/WS_2 moiré superlattices. *Nat. Mater.* **20**, 940–944 (2021).
22. Ghiotto, A. et al. Quantum criticality in twisted transition metal dichalcogenides. *Nature* **597**, 345–349 (2021).
23. Li, T. et al. Quantum anomalous Hall effect from intertwined moiré bands. *Nature* **600**, 641–646 (2021).
24. Gu, J. et al. Dipolar excitonic insulator in a moiré lattice. *Nat. Phys.* **18**, 395–400 (2022).
25. Kira, M. & Koch, S. W. Many-body correlations and excitonic effects in semiconductor spectroscopy. *Prog. Quantum Electron.* **30**, 155–296 (2006).
26. Liu, E. et al. Signatures of moiré trions in $WSe_2/MoSe_2$ heterobilayers. *Nature* **594**, 46–50 (2021).
27. Brotons-Gisbert, M. et al. Moiré-trapped interlayer trions in a charge-tunable $WSe_2/MoSe_2$ heterobilayer. *Phys. Rev.* **11**, 031033 (2021).
28. Wang, X. et al. Moiré trions in $MoSe_2/WSe_2$ heterobilayers. *Nat. Nanotechnol.* **16**, 1208–1213 (2021).
29. Sidler, M. et al. Fermi polaron–polaritons in charge-tunable atomically thin semiconductors. *Nat. Phys.* **13**, 255–261 (2017).
30. Li, H. et al. Imaging moiré flat bands in three-dimensional reconstructed WSe_2/WS_2 superlattices. *Nat. Mater.* **20**, 945–950 (2021).
31. Yu, H., Liu, G.-B. & Yao, W. Brightened spin-triplet interlayer excitons and optical selection rules in van der Waals heterobilayers. *2D Mater.* **5**, 035021 (2018).
32. Schaibley, J. R. et al. Directional interlayer spin-valley transfer in two-dimensional heterostructures. *Nat. Commun.* **7**, 13747 (2016).
33. Zang, J., Wang, J., Cano, J. & Millis, A. J. Hartree–Fock study of the moiré Hubbard model for twisted bilayer transition metal dichalcogenides. *Phys. Rev. B* **104**, 075150 (2021).
34. Hu, N. C. & MacDonald, A. H. Competing magnetic states in transition metal dichalcogenide moiré materials. *Phys. Rev. B* **104**, 214403 (2021).
35. Zhang, Y., Liu, T. & Fu, L. Electronic structures, charge transfer, and charge order in twisted transition metal dichalcogenide bilayers. *Phys. Rev. B* **103**, 155142 (2021).
36. Zhu, Z. & White, S. R. Spin liquid phase of the $S=1/2$ J_1–J_2 Heisenberg model on the triangular lattice. *Phys. Rev. B* **92**, 041105 (2015).
37. Devakul, T., Crépel, V., Zhang, Y. & Fu, L. Magic in twisted transition metal dichalcogenide bilayers. *Nat. Commun.* **12**, 6730 (2021).
38. Pan, H., Wu, F. & Das Sarma, S. Quantum phase diagram of a moiré–Hubbard model. *Phys. Rev. B* **102**, 201104 (2020).
39. Kennes, D. M. et al. Moiré heterostructures as a condensed-matter quantum simulator. *Nat. Phys.* **17**, 155–163 (2021).

Methods

Sample fabrication

Mechanically exfoliated monolayers of WS_2 and WSe_2 were stacked using the dry-transfer technique. Bulk WSe_2 crystals were grown in the laboratory and bulk WS_2 crystals were purchased from HQ Graphene. The crystal orientation of the individual monolayers was first determined by linear-polarization-resolved second-harmonic generation before transfer. All the heterostructures are carefully AFM cleaned with minimal force to obtain a relatively homogeneous sample area. The layer twist angle was determined by PFM before encapsulation with hexagonal boron nitride and graphite. Supplementary Fig. 3a shows a typical PFM image with good homogeneity over a 500 nm range. On the ~10 μm scale, there will be inevitable moiré inhomogeneity, which will be reflected in the PL spectra. For example, a PL map from Device H2 is shown in Supplementary Fig. 3b. Such inhomogeneity would affect the spectral quality but not the conclusion of this work, which is verified across multiple samples.

Optical measurements

PL and differential reflectance measurements were performed using a home-built confocal microscope in reflection geometry. The sample was mounted in a close-cycled cryostat with temperature kept at either 5 K or 10 K, unless otherwise specified. A helium–neon laser (1.96 eV) was used in unpolarized PL measurements. A power-stabilized and frequency-tunable narrow-band continuous-wave titanium–sapphire laser (M^2 SolsTiS) resonant with the WSe_2 1*s* intralayer exciton was used to excite the sample for polarization-resolved PL, with a combination of quarter-wave plates, half-wave plates and linear polarizers. The excitation power for PL measurement is 50–150 nW. For reflection spectroscopy, a halogen lamp was used as a white light source. The output of white light was passed through a single-mode fibre and collimated with a triplet collimator. The beam was then focused onto the sample with a 40× long working distance objective (numerical aperture, 0.6). The excitation power is below 5 nW. Reflectance and PL signals were dispersed by a diffraction grating (600 grooves per mm) and detected on a silicon charge-coupled device camera. The PL was spectrally filtered from the laser using a long-pass filter before being directed into a spectrometer.

Estimation of filling factor based on doping density

The hBN thicknesses of Device R1 are 42 nm (top) and 43 nm (bottom). The hBN thicknesses of Device H1 are 16 nm for both top and bottom gates. The doping density was calculated as $C_t\Delta V_t + C_b\Delta V_b$ based on the parallel-plate capacitance model, where C_t and C_b are the capacitance of the top and bottom gates, and ΔV_t and ΔV_b are the applied gate voltages. $\varepsilon_{hBN} \approx 4$ was used as the dielectric constant of BN in the calculation. The moiré lattice constant was determined by PFM. Doping density and moiré lattice constant were used to initially estimate the filling factors. The filling factors were then compared and adjusted with the assignment of integer filling factors based on optical reflectance measurement (d*R*/*R*) and PL.

First-principles calculations of moiré structures and electronic structures

First-principles calculations were performed using density functional theory with the Perdew–Burke–Ernzerhof functional[40] as implemented in the SIESTA package[41]. The heterobilayer was constructed using 26 × 26 WS_2 and 25 × 25 WSe_2 supercells, where the lattice constants of WS_2 and Wse_2 were taken to be their optimized values, 3.17 Å and 3.30 Å, respectively (within <0.5% error). A supercell arrangement was used, with the out-of-plane axis set to 21 Å to avoid interactions between the moiré heterobilayer and its periodic images. Optimized norm-conserving Vanderbilt pseudopotentials were used[42]. In the relaxation of the structures, the single-zeta basis was chosen and dispersion corrections within the D2 formalism were used to include the van der Waals interactions[43]. The structure was fully relaxed until the force on each atom was <0.03 eV $Å^{-1}$. The normal strain distribution was extracted from the displacement field of tungsten atoms and chalcogen atoms with respect to the unrelaxed heterobilayer. For the calculations of the tungsten-atom strain distribution, the W–W distance was obtained by averaging the distance along six nearest-neighbour tungsten atoms. For the calculations of electronic structure, we used the double-zeta plus polarization basis and spin–orbit coupling.

Modelling exciton–charge–lattice interactions

In the case of small doping density, the exciton–hole–lattice interaction can be approximately treated using screened Coulomb interactions. Thus, the exciton energy shift upon doping relative to the neutral exciton energy can be modelled as the sum of two terms, that is, the attractive interaction between the excitonic electron and the hole lattice, and the repulsive interaction between the excitonic hole and the hole lattice. The potential V_c from the hole lattice acts on the excitonic electron or excitonic hole, having a form

$$V_c(\mathbf{r}) = \sum_{i,\mathbf{R}} \frac{q_i}{4\pi\varepsilon_0\varepsilon_r |\mathbf{r} - \mathbf{r}_i - \mathbf{R}|}$$

where q_i is the charge of the doped hole, $\mathbf{r}_i$ is the position of the doped hole in the primitive unit cell of the hole lattice, and $\mathbf{R}$ is the hole-lattice vector (Fig. 3). As the smallest distance in the denominator of the summation is ~5 nm, much larger than the thickness of the WS_2–WSe_2 heterostructure, ε_r can be taken as the relative permittivity of the environment[37], that is, the encapsulating hBN with $\varepsilon_r \approx 4.0$. To deal with the long-range nature of Coulomb interaction, we adopt the 3D Ewald summation method to rewrite $V_c(r)$ as

$$V_c(\mathbf{r}) = \frac{4\pi}{\Omega}\sum_{i,\mathbf{G}\neq 0} q_i \frac{e^{-G^2/4\alpha^2}}{G^2} e^{-i\mathbf{G}\cdot(\mathbf{r}-\mathbf{r}_i)} + \sum_{i,\mathbf{R}} q_i \frac{\mathrm{erfc}(\alpha|\mathbf{r} - \mathbf{r}_i - \mathbf{R}|)}{|\mathbf{r} - \mathbf{r}_i - \mathbf{R}|}$$

Here, $\mathbf{G}$ is the reciprocal lattice vector and Ω is the volume of the moiré lattice. To avoid artificial interactions from the hole lattice images along the surface normal, a supercell is constructed with large out-of-plane thickness equal to five times the lattice constant of the moiré lattice. The thickness has been tested and converged to ensure the Ewald summation is equivalent to the two-dimensional form. The $\mathbf{G} = 0$ term is skipped in the summation due to compensating charge in the dual gates, which ensures overall charge neutrality. The parameter α is chosen as around 0.003 $Bohr^{-1}$ and the cut-off for the summation over $\mathbf{R}$ and $\mathbf{G}$ is carefully tested for moiré lattices with different filling factors. The doping dependence of exciton energy shift is given in Extended Data Fig. 9 for R- and H-stacked heterobilayers. The energy shift for the electron-doping case is similar.

Reporting summary

Further information on research design is available in the Nature Portfolio Reporting Summary linked to this article.

Data availability

Source data are provided with this paper. All other datasets generated during and/or analysed during this study are available from the corresponding author upon reasonable request. The DFT calculations presented in the paper were carried out using publicly available electronic structure codes (referenced in Methods). Source data are provided with this paper.

References

40. Perdew, J. P., Burke, K. & Ernzerhof, M. Generalized gradient approximation made simple. *Phys. Rev. Lett.* **77**, 3865–3868 (1996).
41. Soler, J. M. et al. The SIESTA method for ab initio order-*N* materials simulation. *J. Phys. Condens. Matter* **14**, 2745–2779 (2002).

42. Hamann, D. R. Optimized norm-conserving Vanderbilt pseudopotentials. *Phys. Rev. B* **88**, 085117 (2013).
43. Grimme, S. Semiempirical GGA-type density functional constructed with a long-range dispersion correction. *J. Comput. Chem.* **27**, 1787–1799 (2006).

Acknowledgements

Research on the exciton many-body ground states is mainly supported by the US Department of Energy (DOE), Office of Science, Basic Energy Sciences (BES) under award DE-SC0018171. Measurements on the R-stacked moiré superlattice are supported as part of Programmable Quantum Materials, an Energy Frontier Research Center funded by the US DOE BES, under award DE-SC0019443. The first-principles calculation is mainly supported by NSF MRSEC DMR-1719797. Computational resources were provided by HYAK at the University of Washington. The theoretical analysis and modelling effort is supported by DOE DE-SC0012509. Device fabrication is partially supported by the Army Research Office (ARO) Multidisciplinary University Research Initiative (MURI) programme (grant number W911NF-18-1-0431). The AFM-related measurements were performed using instrumentation supported by the US National Science Foundation through the UW Molecular Engineering Materials Center (MEM-C), a Materials Research Science and Engineering Center (DMR-1719797). W.Y. acknowledges support by the University Grants Committee/Research Grant Council of Hong Kong SAR (AoE/P-701/20, HKU SRFS2122-7S05) and the Tencent Foundation. Bulk WSe_2 crystal growth and characterization by J.Y. is supported by the US DOE BES, Materials Sciences and Engineering Division. K.W. and T.T. acknowledge support from the Elemental Strategy Initiative conducted by the MEXT, Japan (grant number JPMXP0112101001) and JSPS KAKENHI (grant numbers 19H05790, 20H00354 and 21H05233). T.C. acknowledges support from the Micron Foundation. X.X. acknowledges support from the State of Washington-funded Clean Energy Institute and from the Boeing Distinguished Professorship in Physics. W.G.H. was supported by the NSF Graduate Research Fellowship Program under grant number DGE-1762114.

Author contributions

X.X., W.Y., T.C. and D.X. conceived the project. X.W., H.P. and J.Z. fabricated and characterized the samples. X.W., J.Z., H.P. and Y.W. performed the measurements, assisted by W.G.H. X.W., X.Z., C.W., X.X., W.Y., T.C., D.X. and D.R.G. analysed and interpreted the results. X.Z. and C.W. performed density function calculations. T.T. and K.W. synthesized the hBN crystals. J.Y. synthesized and characterized the bulk WSe_2 crystals. X.X., X.W., X.Z., W.Y., T.C., D.X. and D.R.G. wrote the paper with input from all authors. All authors discussed the results.

Competing interests

The authors declare no competing interests.

Additional information

Extended data is available for this paper at https://doi.org/10.1038/s41563-023-01496-2.

Supplementary information The online version contains supplementary material available at https://doi.org/10.1038/s41563-023-01496-2.

Correspondence and requests for materials should be addressed to Wang Yao, Di Xiao, Ting Cao or Xiaodong Xu.

Peer review information *Nature Materials* thanks Paulina Plochocka and the other, anonymous, reviewer(s) for their contribution to the peer review of this work.

https://doi.org/10.1038/s41563-023-01496-2

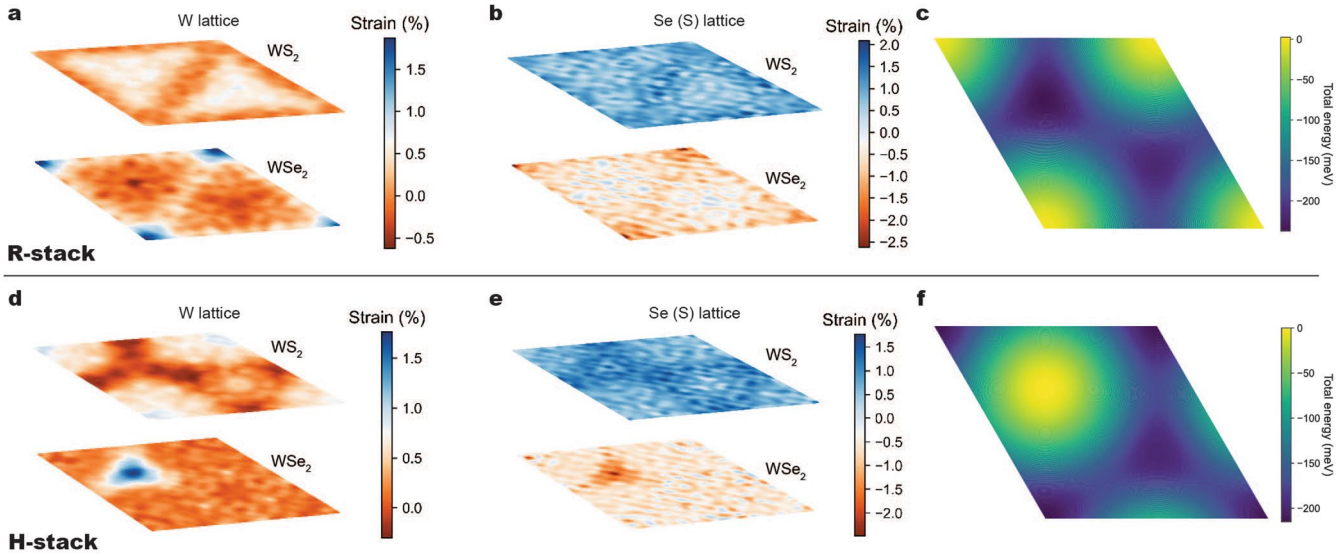

Extended Data Fig. 1 | Calculated normal strain distribution and structural energy of the R- and H-stacked heterobilayers. a, and **d**, Calculated strain maps of the moiré unit cell for the fully relaxed W lattice in WS_2 and WSe_2 layers versus free-standing layers for (**a**) R- and (**d**) H-stacked heterolayers. **b**, and **e**, similar to **a** and **d**, but for the fully relaxed Se or S lattice in the moiré unit cell. The strain distributions are different in R- and H-stacked heterobilayers. Taking A site as the inversion center of the strain distribution as an example, the inversion symmetry weakly breaks in the former, but strongly breaks in the latter. **c** and **f**, Calculated structural energy distribution for the local stacking configuration in the moiré cell for (**c**) R-stacked and (**f**) H-stacked heterobilayers. The different structural energy distributions of local stackings lead to the distinct strain features in **a**-**b**, **d**-**e**.

https://doi.org/10.1038/s41563-023-01496-2

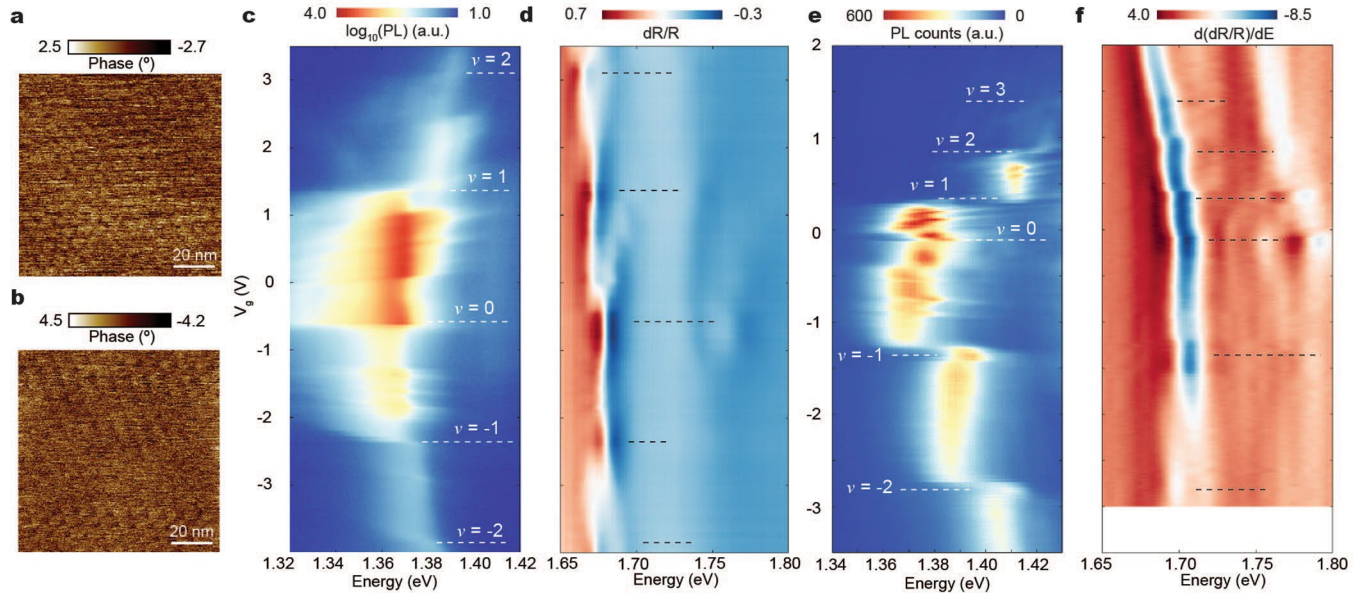

Extended Data Fig. 2 | Moiré filling factor assignment. a-b, PFM image of Device R1 (**a**) and Device H1 (**b**) described in the maintext. The moiré wavelengths are measured as 7.5 nm (R1) and 8 nm (H1). **c**, Gate-dependent interlayer exciton photoluminescence, taken at a different cool down compared to Fig. 2d in the maintext. The excitation energy is 1.96 eV with the power 50 nW. Temperature is 4.7 K. **d**, Corresponding differential optical reflectance spectra of Device R1. **c** and **d** share the same y axis. **e**, Gate-dependent interlayer exciton PL (same as Fig. 4c) of Device H1, and **f**, Corresponding differential optical reflectance spectra differentiated with respect to photon energy. **e** and **f** share the same y axis.

https://doi.org/10.1038/s41563-023-01496-2

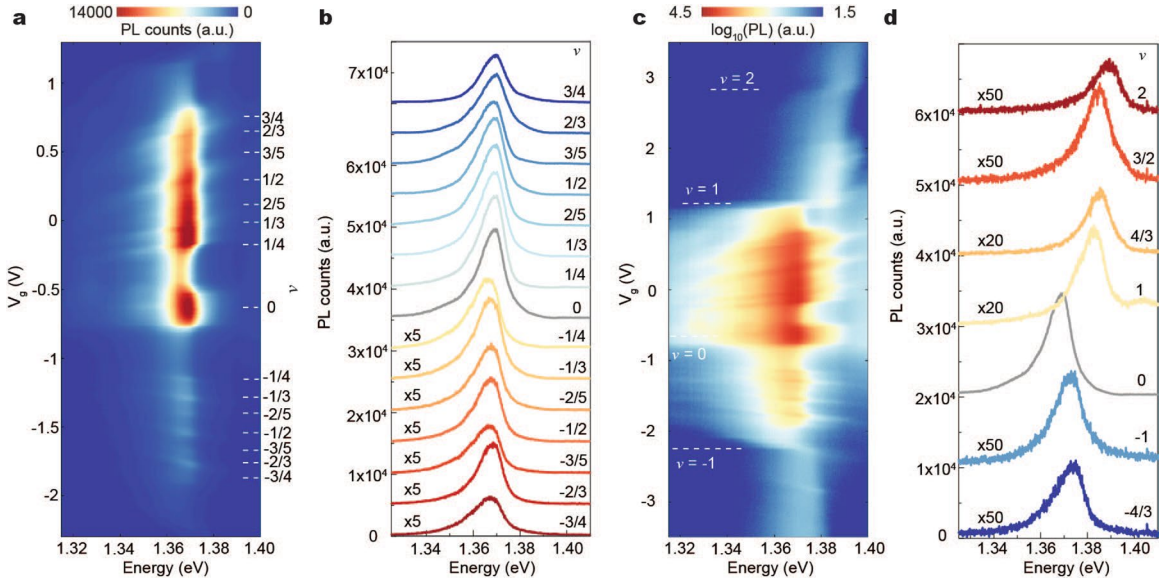

Extended Data Fig. 3 | Interlayer exciton PL of Device R1 at selected filling factors. a, Zoom-in of gate-dependent interlayer exciton PL of Device R1 with $|\upsilon| < 1$. **b**, Linecuts of PL spectra with fractional fillings. The PL spectra are evenly offset. At hole doping side, the PL counts are multiplied by 5 times. There is little variation of PL peak energy as υ varies. **c**, Gate-dependent interlayer exciton PL of Device R1, same as Fig. 2d in main text. **d**, Linecuts of PL spectra at integer filling conditions. The spectra are evenly offset. The PL counts are multiplied by either 20 or 50 times, as indicated in the plot, except at $\upsilon = 0$.

https://doi.org/10.1038/s41563-023-01496-2

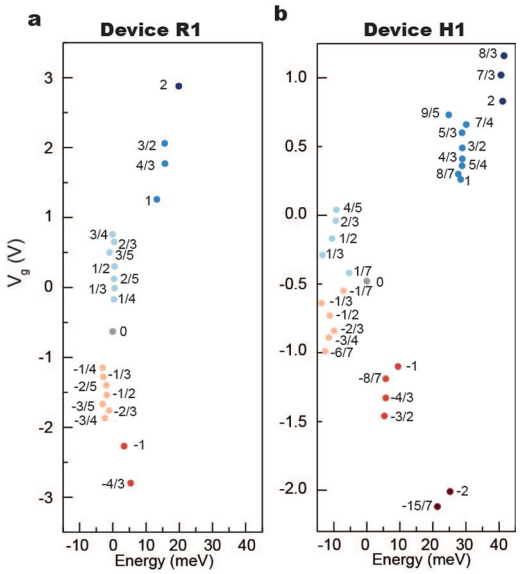

Extended Data Fig. 4 | Relative energy shifts of PL peaks at fractional and integer fillings, with respect to charge neutrality for Device R1 (a) and Device H1 (b).

https://doi.org/10.1038/s41563-023-01496-2

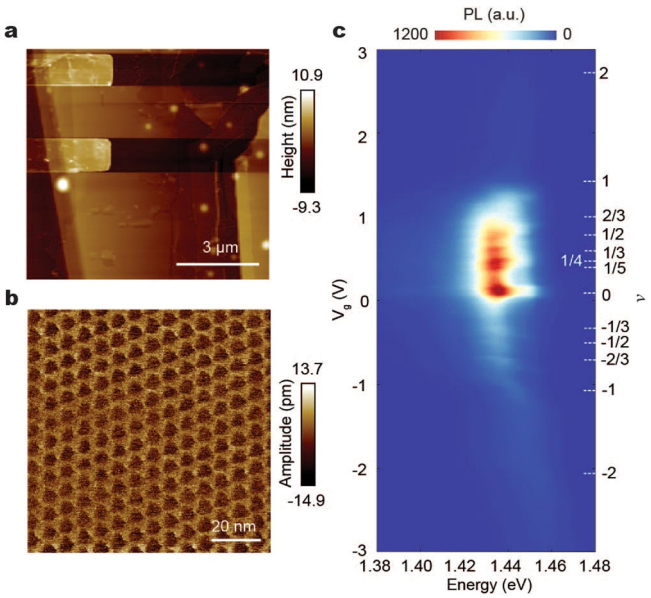

Extended Data Fig. 5 | Additional R-stacked heterobilayer Device R2. a, AFM morphology and **b**, PFM image of Device R2, showing the moiré wavelength is about 7.5 nm**. c**. Gate-dependent interlayer exciton photoluminescence of Device R2, with filling factors indicated.

https://doi.org/10.1038/s41563-023-01496-2

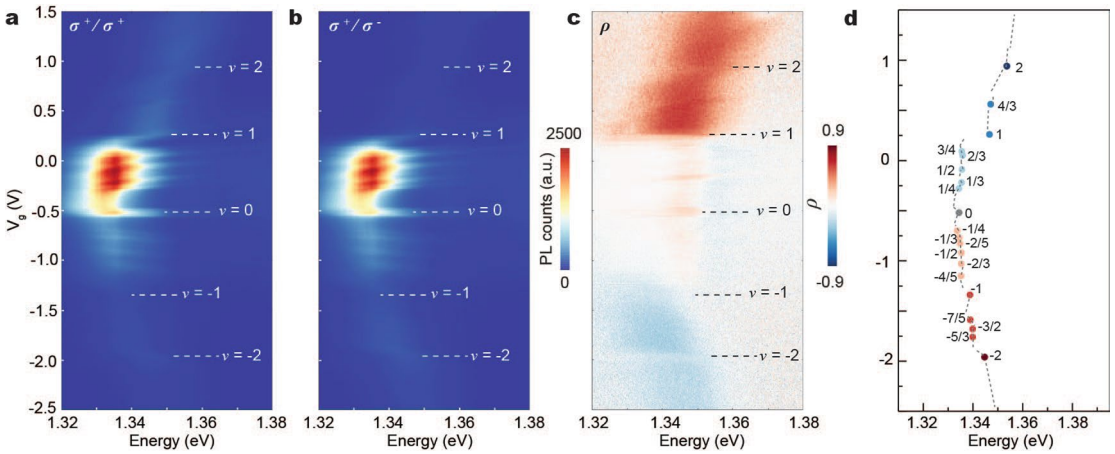

Extended Data Fig. 6 | Polarization resolved PL of an additional R-stacked heterobilayer Device R3. a, Co-circularly **b**, cross-circularly polarized interlayer exciton PL for Device R3 under σ+ circularly polarized excitation. The excitation power is 60 nW with excitation energy 1.682 eV at 10 K. **c**, Corresponding degree of circularly polarization ρ. a-c share the same y axis. **d**, Extracted PL peak energies (dots) for each integer and fractionally filled correlated charge states. The dashed lines indicate PL peak energies at all measured gate voltages. Devices R3 and H2 (Extended Data Fig. 8) are different parts of the same sample.

https://doi.org/10.1038/s41563-023-01496-2

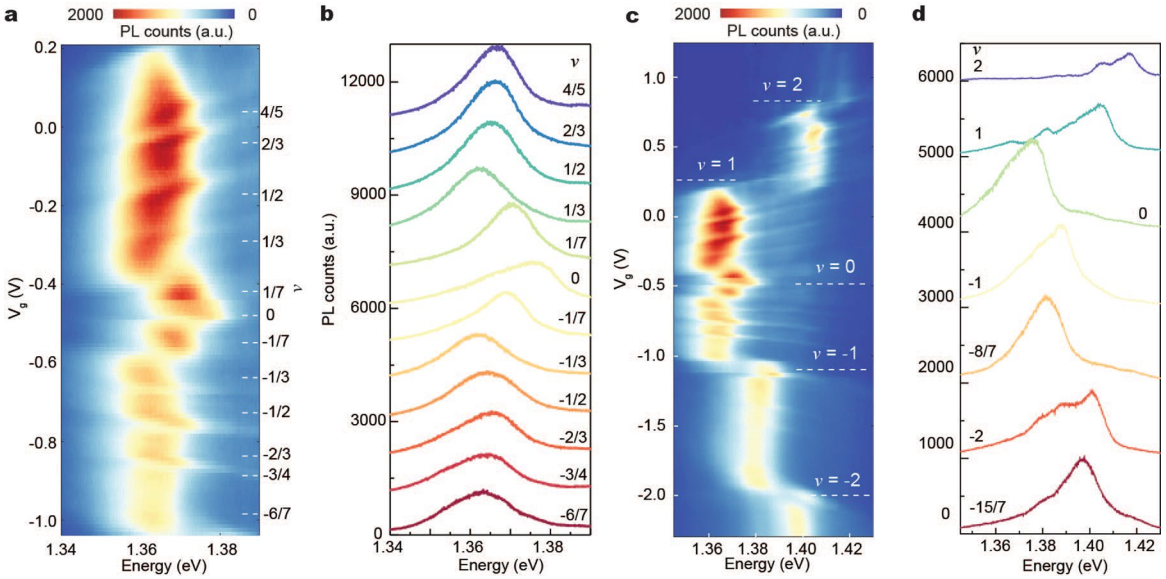

Extended Data Fig. 7 | PL spectra of Device H1 at select filling factors. a, Zoom-in of gate-dependent interlayer exciton PL with $|\nu| < 1$. **b**, Linecuts of PL spectra at fractional filling conditions as marked. **c**, Gate-dependent interlayer exciton PL, same as Fig. 2f in main text. **d**, Linecuts of PL spectra at integer and select fractional fillings. The spectra in **b** and **d** are evenly offset for clarity. The numbers of charge carriers required to form adjacent charge orders with fractional filling factors are close. At the transition regime between two adjacent charge orders, it is possible that domains with different charge orders form. The charge order domains may be responsible for the observed multiple peaks in spectra at certain doping conditions.

https://doi.org/10.1038/s41563-023-01496-2

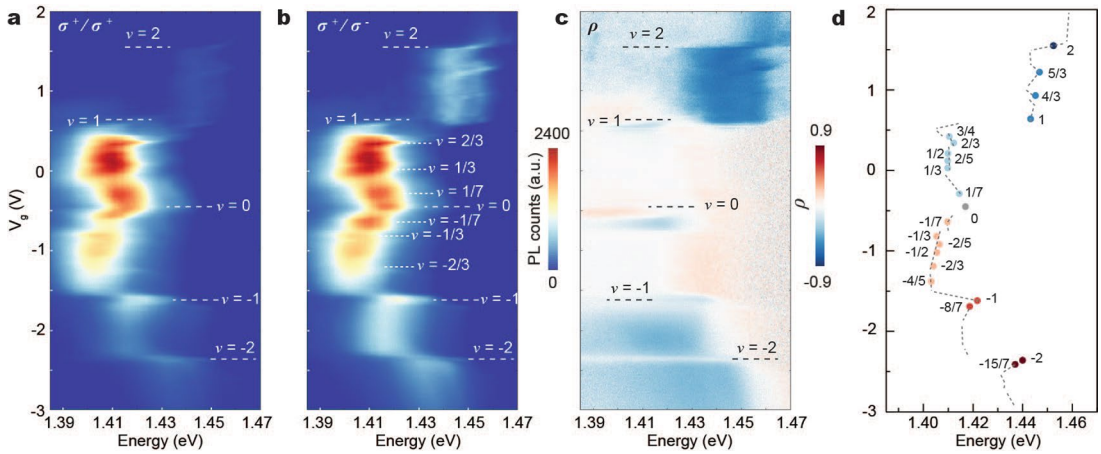

Extended Data Fig. 8 | Polarization resolved PL of an additional H-stacked heterobilayer Device H2. a, Co-circularly **b**, cross-circularly polarized interlayer exciton PL for Device H2 under σ + circularly polarized excitation. The excitation power is 60 nW with excitation energy 1.682 eV at 10 K. **c**, Corresponding degree of circularly polarization ρ. **a**–**c** share the same y axis. **d**, Extracted PL peak energies (dots) for each integer and fractionally filled correlated charge states. The dashed lines indicate PL peak energies at all measured gate voltages. Devices R3 (Extended Data Fig. 6) and H2 are different parts of the same sample.

https://doi.org/10.1038/s41563-023-01496-2

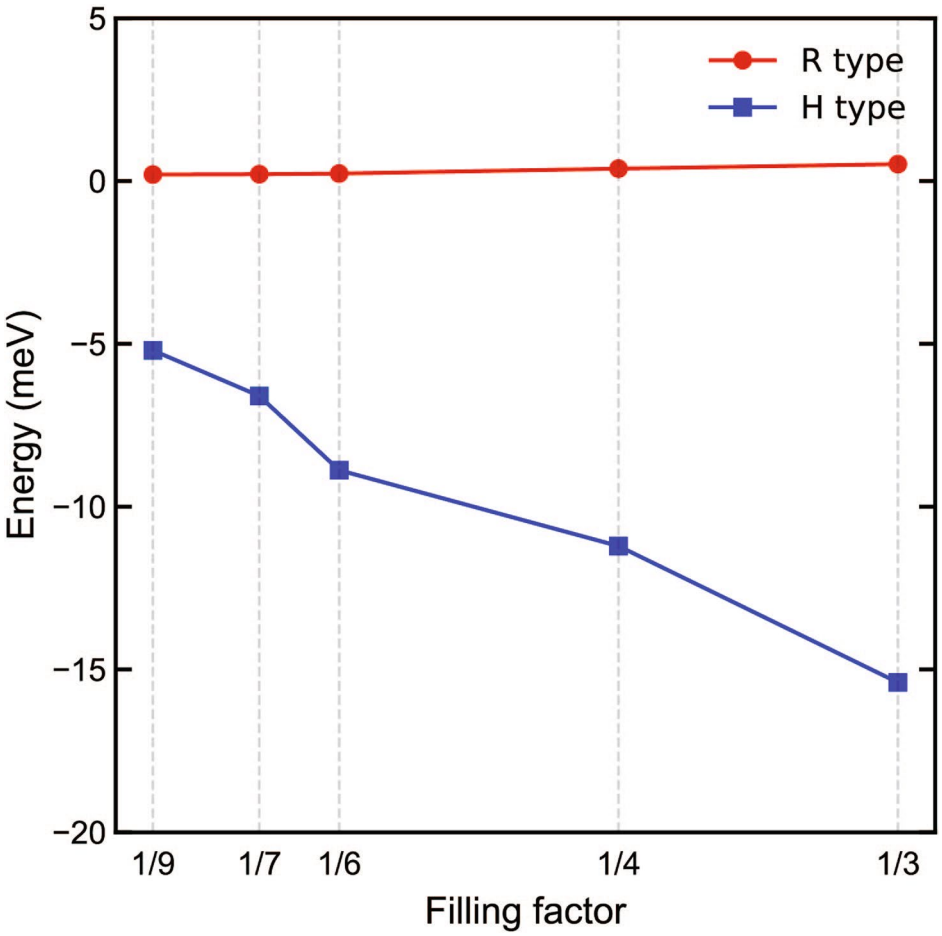

Extended Data Fig. 9 | Calculated Coulomb interaction energy between the exciton and electron-lattice for the filling factors ≤1/3. Standard Ewald summation technique is used to calculate the Coulomb interaction energies for different filling factors. The convergence parameters have been carefully tested when doing the summation. The collective interaction is repulsive for R stacking and attractive for H stacking.

https://doi.org/10.1038/s41563-023-01496-2

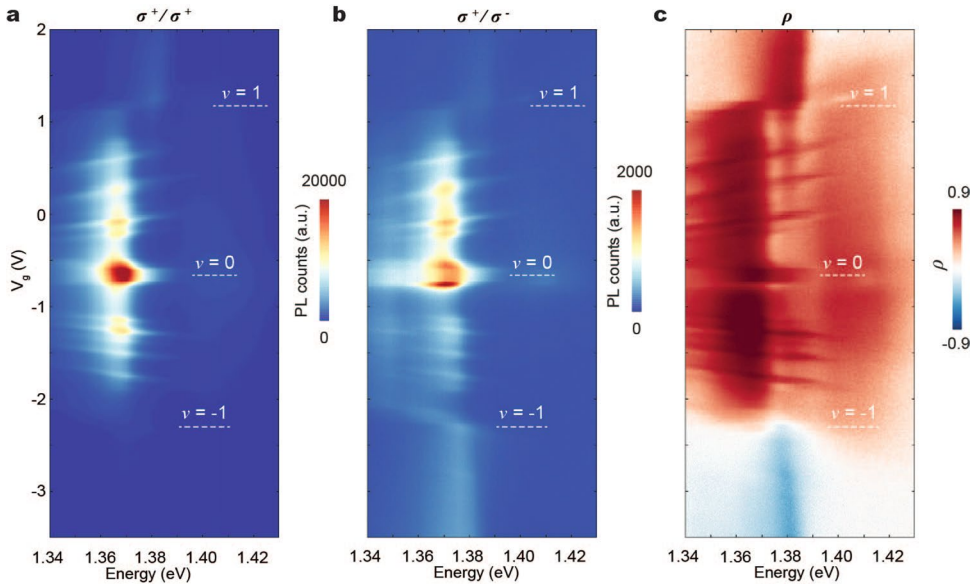

Extended Data Fig. 10 | Polarization resolved PL of Device R1 at a magnetic field of 8 T. a, Co-circularly and **b**, Cross-circularly polarized interlayer exciton PL under $\sigma+$ circularly polarized pump. **c**, The corresponding degree of circularly polarization ρ. Data is taken at 15 K. The optical excitation power is 300 nW with excitation energy at 1.678 eV.

nature portfolio

Corresponding author(s): Xiaodong Xu

Last updated by author(s): Jan 29, 2023

Reporting Summary

Nature Portfolio wishes to improve the reproducibility of the work that we publish. This form provides structure for consistency and transparency in reporting. For further information on Nature Portfolio policies, see our Editorial Policies and the Editorial Policy Checklist.

Statistics

For all statistical analyses, confirm that the following items are present in the figure legend, table legend, main text, or Methods section.

n/a	Confirmed
☐	☒ The exact sample size (*n*) for each experimental group/condition, given as a discrete number and unit of measurement
☐	☒ A statement on whether measurements were taken from distinct samples or whether the same sample was measured repeatedly
☒	☐ The statistical test(s) used AND whether they are one- or two-sided *Only common tests should be described solely by name; describe more complex techniques in the Methods section.*
☐	☒ A description of all covariates tested
☐	☒ A description of any assumptions or corrections, such as tests of normality and adjustment for multiple comparisons
☒	☐ A full description of the statistical parameters including central tendency (e.g. means) or other basic estimates (e.g. regression coefficient) AND variation (e.g. standard deviation) or associated estimates of uncertainty (e.g. confidence intervals)
☒	☐ For null hypothesis testing, the test statistic (e.g. *F*, *t*, *r*) with confidence intervals, effect sizes, degrees of freedom and *P* value noted *Give P values as exact values whenever suitable.*
☒	☐ For Bayesian analysis, information on the choice of priors and Markov chain Monte Carlo settings
☒	☐ For hierarchical and complex designs, identification of the appropriate level for tests and full reporting of outcomes
☒	☐ Estimates of effect sizes (e.g. Cohen's *d*, Pearson's *r*), indicating how they were calculated

Our web collection on statistics for biologists contains articles on many of the points above.

Software and code

Policy information about availability of computer code

Data collection	The DFT calculations presented in the paper were carried out using publicly available electronic structure codes (referenced in the Methods section), with the Perdew-Burke-Ernzerhof functional as implemented in the SIESTA package.
Data analysis	The DFT calculations presented in the paper were carried out using publicly available electronic structure codes (referenced in the Methods section).

For manuscripts utilizing custom algorithms or software that are central to the research but not yet described in published literature, software must be made available to editors and reviewers. We strongly encourage code deposition in a community repository (e.g. GitHub). See the Nature Portfolio guidelines for submitting code & software for further information.

Data

Policy information about availability of data

All manuscripts must include a data availability statement. This statement should provide the following information, where applicable:

- Accession codes, unique identifiers, or web links for publicly available datasets
- A description of any restrictions on data availability
- For clinical datasets or third party data, please ensure that the statement adheres to our policy

Source data are provided with this paper. The DFT calculations presented in the paper were carried out using publicly available electronic structure codes (referenced in the Methods section).

Human research participants

Policy information about studies involving human research participants and Sex and Gender in Research.

Reporting on sex and gender	N/A
Population characteristics	N/A
Recruitment	N/A
Ethics oversight	N/A

Note that full information on the approval of the study protocol must also be provided in the manuscript.

Field-specific reporting

Please select the one below that is the best fit for your research. If you are not sure, read the appropriate sections before making your selection.

☐ Life sciences ☐ Behavioural & social sciences ☒ Ecological, evolutionary & environmental sciences

For a reference copy of the document with all sections, see nature.com/documents/nr-reporting-summary-flat.pdf

Ecological, evolutionary & environmental sciences study design

All studies must disclose on these points even when the disclosure is negative.

Study description	we report a new interaction between exciton and charges enabled by unusual quantum confinement in in H-stacked (i.e., 60o-twisted) WS2/WSe2 moiré superlattices. Upon doping, the electric quadrupole facilitates the binding of intercell exciton (IME) to the charges in neighboring moiré cells, forming an intercell charged exciton complex. The exciton complex is unveiled by the IME photoluminescence energy jumps when the electron lattices form at both fractional and integer-filled moiré minibands, with replica-like spectral features between successive integer moiré fillings.
Research sample	WS2/WSe2 moiré heterobilayers as described in the maintexts.
Sampling strategy	Repeated samples as described in maintexts and extended data figures.
Data collection	XW, JZ, HP and YW performed the measurements, assisted by WH. XW, XZ, CW, XX, WY, TC, DX, DRG analyzed and interpreted the results. XZ and CW performed density function calculations. TT and KW synthesized the hBN crystals. JY synthesized and characterized the bulk WSe2 crystals.
Timing and spatial scale	The data was collected starting in July, 2021
Data exclusions	N/A
Reproducibility	Reproduced through multiple samples included in the manuscript and extended data figures.
Randomization	The sample fabrication is controlled.
Blinding	N/A

Did the study involve field work? ☐ Yes ☒ No

Reporting for specific materials, systems and methods

We require information from authors about some types of materials, experimental systems and methods used in many studies. Here, indicate whether each material, system or method listed is relevant to your study. If you are not sure if a list item applies to your research, read the appropriate section before selecting a response.

Materials & experimental systems

n/a	Involved in the study
☒	☐ Antibodies
☒	☐ Eukaryotic cell lines
☒	☐ Palaeontology and archaeology
☒	☐ Animals and other organisms
☒	☐ Clinical data
☒	☐ Dual use research of concern

Methods

n/a	Involved in the study
☒	☐ ChIP-seq
☒	☐ Flow cytometry
☒	☐ MRI-based neuroimaging